Optically controlled quantum thermal gate

Ravi T. Wijesekara,[1,*] Sarath D. Gunapala,[2] Mark I. Stockman,[3] and Malin Premaratne[1,†]

[1]*Advanced Computing and Simulation Laboratory(AχL), Department of Electrical and Computer Systems Engineering, Monash University, Clayton, Victoria 3800, Australia*

[2]*Jet Propulsion Laboratory, California Institute of Technology, Pasadena, California 91109, USA*

[3]*Department of Physics and Astronomy, Georgia State University, Atlanta, Georgia 30303, USA*

(Received 25 February 2020; revised manuscript received 19 April 2020; accepted 13 May 2020; published 1 June 2020)

The ability to actively control heat flows in the nanoscale can open up a plethora of opportunities for applications that require thermal management and regulation. We show that it is possible to build a three-terminal quantum thermal gating device which regulates the thermal conductivity between two of its terminals in response to light incident upon the remaining terminal. We model our device as three mutually coupled two-level systems which interact thermally and optically with their environment. To incorporate the thermal interactions of our device, we adopt an open quantum systems framework under the Born-Markov approximation. We subsequently use detailed quantum mechanical state analysis to illustrate its operating principle. Through numerical simulations, we further explore the nonlinear relationship between the optical field amplitude and the thermal conductivity of the device in the steady-state regime. Based on our investigations, we find that the energy-gating behavior of our device is highly efficient in that it can control a significantly larger thermal energy flow compared to the amount of energy it absorbs from the optical field in the process. The approach we have taken to analyze the system, in particular the graphical representations we developed to intuitively and concisely represent the quantum states, energy flows, and the relationships between them, could be of value in analyzing other similar thermo-optical systems. Thus, we envision that both the device concept and its analysis technique would be useful to researchers working in this area.

DOI: 10.1103/PhysRevB.101.245402

I. INTRODUCTION

Considerable research effort in recent years has been devoted to synthesizing materials whose thermal conductivity can be regulated using an external control signal. Such materials that can control the heat transfer through systems can find a myriad of interdisciplinary applications [1,2]. For example, these materials would be instrumental in developing reconfigurable thermal routing networks, controllable thermal insulators, thermal rectifiers, and improved waste heat management and energy harvesting systems for semiconductor devices [3,4].

A polymer-based light-sensitive thermal conductivity-adjustable material (TCAM) was recently reported in Ref. [5], where absorption of ultraviolet radiation of a specific wavelength induces a reversible phase change [6] in the polymer, which in turn alters its thermal conductivity. Magnetic and electric field sensitive materials reported in Refs. [1,7] similarly alter their conductivity through changes to their internal chemical structure. These and other similar works follow a macroscale approach to developing TCAMs.

However, recent advances in nanotechnology has made possible the development of devices which manipulate individual quantum systems such as quantum dots [8], quantum emitters [9] and nanoparticles [10]. Rectification and switching devices for electrons [11,12], photons [13–16] or phonons [17,18], electrically controlled phonon gating devices [19], spasers [20,21], and single photon detectors [22] or emitters [23] are some examples for such quantum technologies.

Important among these is the development of quantum thermal rectifiers [24,25] and transistors [26–29]. A thermal rectifier conducts heat along one preferred direction and insulates heat along the opposite direction, while a thermal transistor regulates the conductivity along two of its terminals in response to the temperature of its third (gate) terminal. Both these examples offer nanoscale mechanisms to control heat flow and opens a new approach for developing TCAMs, where we build macroscale thermal materials by systematically assembling nanoscale thermal devices.

However, there are still serious challenges to overcome in integrating a large number of such thermal devices within a larger system. Foremost among them is the problem of giving accurate and localized control signals to each individual device. This is especially difficult since almost all currently proposed thermal devices are controlled by temperature signals, which are quite difficult to synthesize and efficiently guide to relevant locations in nanoscale circuitry [30]. Developing quantum thermal devices controlled by alternative mechanisms, such as light or voltage, would circumnavigate this problem.

In this work, we propose a three-terminal thermal gating device whose thermal conductivity between two of its terminals can be modulated via a light of specific wavelength

*ravi.wijesekara@monash.edu

†malin.premaratne@monash.edu

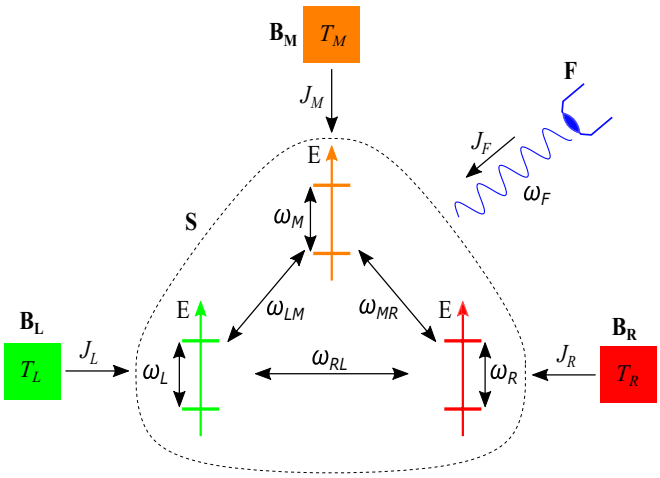

FIG. 1. Quantum system demonstrating optically controllable thermal gating behavior. T_P is the temperature of the thermal bath B_P, J_P is the energy flow rate from B_P to S for $P = L,\ M,$ and R, and J_F is the energy absorption rate of S from the field F.

shining on its third terminal. The operation is similar to that of the quantum thermal transistor developed by Joulain *et al.* [26], except that the device is now optically controlled as opposed to temperature controlled. We believe by introducing optical control, we will drastically expand the usability and improve the accuracy of current thermal flow-control devices. Furthermore, we believe the mechanism of optical control we use here, and our methods for analysis and visual depiction of the operating principle, would be readily adaptable for other similar problems in quantum thermal science.

Our paper is organized as follows. In Sec. II, we introduce our quantum system and the formalism we use for analyzing its thermal behavior. In Sec. III, we discuss the time evolution of the system quantum state and its thermal properties, concentrating particularly on the steady-state situation after transients due to initial conditions have died out. We numerically simulate and present the behaviors of the system in Sec. IV, demonstrating that optically controlled thermal gating behavior is indeed shown by our quantum device. The mechanism of how our device operates is explained in detail in Sec. V. Finally we summarize our findings and conclude our discussion in Sec. VI.

II. MODEL

Our system is an extension of the quantum thermal transistor analyzed in Ref. [26] and consists of three mutually coupled two-level systems (TLSs), three thermal baths interacting with the TLSs, and an additional single-mode optical field (Fig. 1). In our analysis, the three TLSs, labeled by L (left), M (mid), and R (right), together form the system S, and their three corresponding thermal baths (B_L, B_M and B_R) form its environment. The optical field (labeled F) is imposed on all three TLSs of our system. However, as we shall discuss in the subsequent section, we specifically tune the frequency of the field ω_F and the system parameters of S such that the optical field strongly interacts only with the TLS M.

Our goal now is to analyze the bath-system energy flows J_L, J_M, J_R and field-system energy flow J_F using the strong-coupling formalism employed in Werlang *et al.* [24]. We concentrate specifically on the effect of the amplitude of field F on the energy flows between the thermal baths and the system. Joulain *et al.* [26] previously found that under certain conditions the energy flow (i.e., thermal conductivity) between thermal reservoirs B_L and B_R could be accurately controlled by tuning the temperature of the reservoir B_M, very much like the operation of an electronic field effect transistor (FET). Alternatively, in this work we show that by coupling an optical field F and adjusting its amplitude, we can similarly control the thermal conductivity between B_L and B_R. Moreover, we show that the energy absorption of S from F turns out to be at least an order of magnitude smaller than the system-bath energy flows it regulates. We thereby demonstrate that our system acts as an energy-efficient optically controlled thermal gating device.

A. System, bath, and field Hamiltonians

Each TLS can be in one of two possible energy eigenstates, which we denote $|{\uparrow_P}\rangle$ and $|{\downarrow_P}\rangle$ for $P = L,\ M,$ and R. The Hilbert space of S then becomes the tensor product space of the three individual TLSs.

We can now write the Hamiltonian of the system S as an 8×8 matrix

$$\hat{H}_S = \frac{\hbar}{2}\big(\omega_L\hat{\sigma}_z^L + \omega_M\hat{\sigma}_z^M + \omega_R\hat{\sigma}_z^R + \omega_{LM}\hat{\sigma}_z^L\hat{\sigma}_z^M + \omega_{MR}\hat{\sigma}_z^M\hat{\sigma}_z^R + \omega_{RL}\hat{\sigma}_z^R\hat{\sigma}_z^L\big), \quad (1)$$

where $\hbar$ is the reduced Planck constant, $\hbar\omega_P$ is the energy difference between the two eigenstates of TLS P, and $\hbar\omega_{PQ}$ is the interaction energy between the TLSs P and Q for $P, Q = \{L, M, R\}$. Here $\hat{\sigma}_z^P$ is the third Pauli matrix for TLS P expanded into an 8×8 space by appropriate tensor products with unit matrices [31]. For example, $\hat{\sigma}_z^L = \hat{\sigma}_z \otimes \hat{I} \otimes \hat{I}$ where $\hat{\sigma}_z$ is the 2×2 Pauli matrix and $\hat{I}$ is the 2×2 unit matrix.

Diagonalizing the matrix H_S provides the following energy eigenvectors $|j\rangle$ and corresponding eigenvalues ϵ_j

$$|1\rangle \equiv |{\uparrow\uparrow\uparrow}\rangle \leftrightarrow \frac{\hbar}{2}(+\omega_L + \omega_M + \omega_R + \omega_{LM} + \omega_{MR} + \omega_{RL}),$$

$$|2\rangle \equiv |{\uparrow\uparrow\downarrow}\rangle \leftrightarrow \frac{\hbar}{2}(+\omega_L + \omega_M - \omega_R + \omega_{LM} - \omega_{MR} - \omega_{RL}),$$

$$|3\rangle \equiv |{\uparrow\downarrow\uparrow}\rangle \leftrightarrow \frac{\hbar}{2}(+\omega_L - \omega_M + \omega_R - \omega_{LM} - \omega_{MR} + \omega_{RL}),$$

$$|4\rangle \equiv |{\uparrow\downarrow\downarrow}\rangle \leftrightarrow \frac{\hbar}{2}(+\omega_L - \omega_M - \omega_R - \omega_{LM} + \omega_{MR} - \omega_{RL}),$$

$$|5\rangle \equiv |{\downarrow\uparrow\uparrow}\rangle \leftrightarrow \frac{\hbar}{2}(-\omega_L + \omega_M + \omega_R - \omega_{LM} + \omega_{MR} - \omega_{RL}),$$

$$|6\rangle \equiv |{\downarrow\uparrow\downarrow}\rangle \leftrightarrow \frac{\hbar}{2}(-\omega_L + \omega_M - \omega_R - \omega_{LM} - \omega_{MR} + \omega_{RL}),$$

$$|7\rangle \equiv |{\downarrow\downarrow\uparrow}\rangle \leftrightarrow \frac{\hbar}{2}(-\omega_L - \omega_M + \omega_R + \omega_{LM} - \omega_{MR} - \omega_{RL}),$$

$$|8\rangle \equiv |{\downarrow\downarrow\downarrow}\rangle \leftrightarrow \frac{\hbar}{2}(-\omega_L - \omega_M - \omega_R + \omega_{LM} + \omega_{MR} + \omega_{RL}),$$

where $|{\uparrow\uparrow\uparrow}\rangle = |{\uparrow_L}\rangle \otimes |{\uparrow_M}\rangle \otimes |{\uparrow_R}\rangle$ and so on.

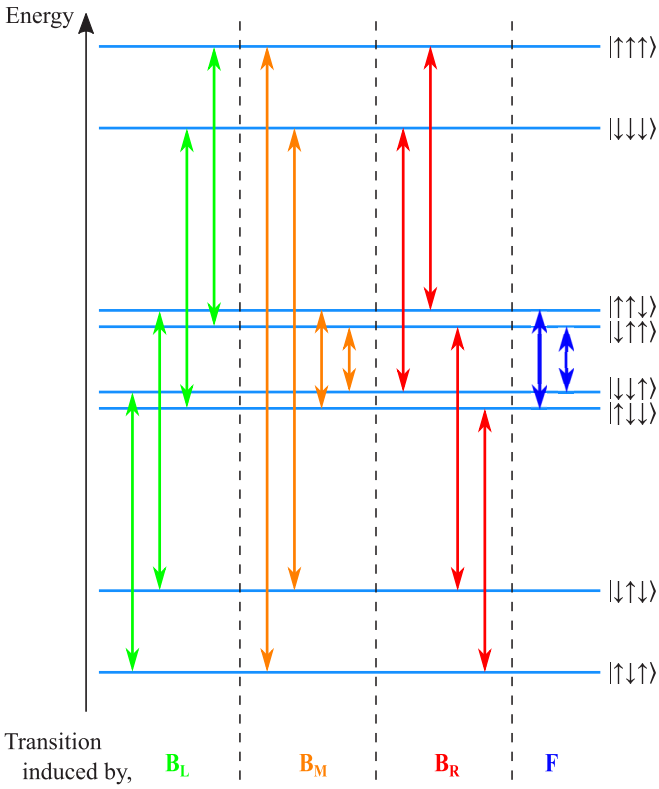

FIG. 2. Energy eigenstates and eigenvalues for S with typical system parameters for operating as an optically controlled thermal gate ($\omega_L = \omega_R = \omega_{RL} = 0$, $\omega_{LM} \approx \omega_{MR} \gg \omega_M$). Arrows indicate allowed energy transitions while their colors represent the external entity the energy is exchanged with.

The energy level diagram of the system S for a typical set of parameters ω_P and ω_{PQ} is shown in Fig. 2. Note that with our convention, when ω_P and ω_{PQ} are positive, $|\uparrow_P\rangle$ has higher energy than $|\downarrow_P\rangle$, and the interaction between TLSs P and Q generates higher energy when both arrows align than when they are opposite.

Following the methodology of the well-established Caldeira-Leggett model [32], we consider all three thermal reservoirs as collections of quantum harmonic oscillators. Hence, we write their Hamiltonians as

$$\hat{H}^P_{\text{bath}} = \sum_k \hbar\omega_k \, \hat{a}_k^{P\,\dagger} \hat{a}_k^P, \tag{2}$$

where $\hat{a}_k^P$ is the annihilation operator for the oscillation mode with frequency ω_k of reservoir P.

We model the interaction Hamiltonian $\hat{H}^P_{\text{TLS-bath}}$ between the TLS P and its respective thermal bath following the arguments in Leggett *et al.* [33]. We therefore consider the interaction to link the energy of the TLS P to the position of each quantum harmonic oscillator in the respective bath. This yields

$$\hat{H}^P_{\text{TLS-bath}} = \hbar\hat{\sigma}_x^P \sum_k g_k \left(\hat{a}_k^P + \hat{a}_k^{P\,\dagger}\right), \tag{3}$$

where g_k represents the coupling strength between the thermal bath's k^{th} oscillation mode and the TLS, and is assumed to be equal for all three reservoirs for simplicity. Note that as a consequence of the TLSs only interacting with their corresponding thermal reservoirs, an energy exchange between the system and any one thermal bath can only flip the quantum state of its corresponding TLS. This constraints the number of allowed transitions within S to twelve, with four transitions induced by each reservoir as shown in Fig. 2.

We model the external optical field F classically and write its electric field component $\vec{E}(t)$ incident on the system S at time t as

$$\vec{E}(t) = \vec{E}_0 \cos\omega_F t, \tag{4}$$

where $|\vec{E}_0|$ and ω_F are respectively the amplitude and frequency of the optical field. Under the dipole approximation [34], the interaction Hamiltonian between the field and the system is

$$\begin{aligned}\hat{H}_{\text{S-F}} &= -\sum_{P=L,M,R} \hat{\vec{D}}^P \cdot \vec{E}(t) \\ &= -\sum_{P=L,M,R} \vec{d}(\hat{\sigma}_+^P + \hat{\sigma}_-^P) \cdot \vec{E}_0 \cos\omega_F t \\ &= -\sum_{P=L,M,R} \hbar\frac{\Omega}{2}(\hat{\sigma}_+^P + \hat{\sigma}_-^P)(e^{-i\omega_F t} + e^{i\omega_F t}),\end{aligned} \tag{5}$$

where $\hat{\sigma}_+^P = \frac{1}{2}(\hat{\sigma}_x^P + i\hat{\sigma}_y^P)$, $\hat{\sigma}_-^P = \frac{1}{2}(\hat{\sigma}_x^P - i\hat{\sigma}_y^P)$, and $\Omega = \frac{\vec{E}_0\cdot\vec{d}}{\hbar}$ is the Rabi frequency. It is important to note that in this work, we will be changing the magnitude of the electric field $|\vec{E}_0|$, while always keeping the dipole moment $\vec{d}$ constant. Since this means that $\Omega \propto |\vec{E}_0|$, in the following sections we will be frequently using Ω instead of $|\vec{E}_0|$ to represent the amplitude of the field, for ease of notation.

In this current form, the interaction $\hat{H}_{\text{S-F}}$ drives all twelve allowed transitions in the system S. However, we note that since these transitions have different energy levels and therefore different resonant frequencies, a single frequency optical field cannot resonate with all of them simultaneously. In essence, if we fine-tune ω_F to be resonant with one particular energy transition, it will likely become nonresonant with all other transitions with different frequencies. The field will then strongly drive the resonant transition, while interacting only weakly with other nonresonant transitions. By carefully choosing our system parameters ω_Ps and ω_{PQ}s, we can exploit this property to suppress most of the transitions in Eq. (5) and significantly simplify $\hat{H}_{\text{S-F}}$.

For instance, in the energy level diagram Fig. 2, we have specifically chosen system parameters so that the transitions $|\uparrow\uparrow\downarrow\rangle \leftrightarrow |\uparrow\downarrow\downarrow\rangle$ and $|\downarrow\uparrow\uparrow\rangle \leftrightarrow |\downarrow\downarrow\uparrow\rangle$ have considerably lower resonant frequencies than any of the other ten allowed transitions. Choosing ω_F to be resonant with the above two transitions by setting $\omega_F = \omega_M + \omega_{LM} - \omega_{MR} = \omega_M - \omega_{LM} + \omega_{MR}$, we can then ignore the nonresonant high-frequency transitions in $\hat{H}_{\text{S-F}}$. This leaves us with a simplified interaction Hamiltonian,

$$\begin{aligned}\hat{H}_{\text{S-F}} = -\hbar\frac{\Omega}{2}(&|\uparrow\uparrow\downarrow\rangle\langle\uparrow\downarrow\downarrow| + |\uparrow\downarrow\downarrow\rangle\langle\uparrow\uparrow\downarrow| + |\downarrow\uparrow\uparrow\rangle\langle\downarrow\downarrow\uparrow| \\ &+ |\downarrow\downarrow\uparrow\rangle\langle\downarrow\uparrow\uparrow|)(e^{-i\omega_F t} + e^{i\omega_F t}).\end{aligned} \tag{6}$$

We can map this Hamiltonian to its interaction picture representation $\hat{H}_{\text{S-F}}(t)$ as

$$\begin{aligned}\hat{H}_{\text{S-F}}(t) &= \exp\left\{\frac{i}{\hbar}\hat{H}_{\text{S}}t\right\}\hat{H}_{\text{S-F}}\exp\left\{-\frac{i}{\hbar}\hat{H}_{\text{S}}t\right\}\\ &= -\hbar\frac{\Omega}{2}\Big(\big(|\uparrow\uparrow\downarrow\rangle\langle\uparrow\downarrow\downarrow|+|\downarrow\uparrow\uparrow\rangle\langle\downarrow\downarrow\uparrow|\big)\big(1+e^{i2\omega_F t}\big)\\ &\quad+\big(|\uparrow\downarrow\downarrow\rangle\langle\uparrow\uparrow\downarrow|+|\downarrow\downarrow\uparrow\rangle\langle\downarrow\uparrow\uparrow|\big)\big(1+e^{-i2\omega_F t}\big)\Big).\end{aligned} \tag{7}$$

By performing the rotating wave approximation (RWA) [31,35] we can remove the rapidly oscillating terms $e^{i2\omega_F t}$ and $e^{-i2\omega_F t}$ to obtain

$$\begin{aligned}\hat{H}_{\text{S-F}}(t) = -\hbar\frac{\Omega}{2}&(|\uparrow\uparrow\downarrow\rangle\langle\uparrow\downarrow\downarrow|+|\uparrow\downarrow\downarrow\rangle\langle\uparrow\uparrow\downarrow|\\ &+|\downarrow\uparrow\uparrow\rangle\langle\downarrow\downarrow\uparrow|+|\downarrow\downarrow\uparrow\rangle\langle\downarrow\uparrow\uparrow|).\end{aligned} \tag{8}$$

We note from Eq. (8) that both transitions driven by the field F shifts only the quantum state of the TLS M. This aligns with our earlier statement that our field strongly interacts only with the TLS M.

The combined Hamiltonian of the system and its environment $\hat{H}$ is the sum of its components. Therefore we write

$$\hat{H} = \hat{H}_0 + \hat{H}_1, \tag{9}$$

where we define

$$\hat{H}_0 = \hat{H}_{\text{S}} + \sum_{P=L,M,R}\hat{H}^P_{\text{bath}} \tag{10}$$

to represent the sum of individual energies of the system and its environment, and

$$\hat{H}_1 = \hat{H}_{\text{S-F}} + \sum_{P=L,M,R}\hat{H}^P_{\text{TLS-bath}} \tag{11}$$

to represent the energy of the interactions in between them. In all subsequent sections, we will be working in the interaction picture obtained with respect to $\hat{H}_0$ and $\hat{H}_1$.

B. Quantum master equation

The state of the system S at any time t is completely specified by its 8×8 density matrix $\hat{\rho}(t)$, whose time evolution obeys a quantum master equation. We derive this quantum master equation following the procedure outlined in Appendix A. Under Born, Markov, and RWA approximations [36], this yields the following interaction picture quantum master equation in Lindblad form:

$$\frac{d\hat{\rho}(t)}{dt} = -\frac{i}{\hbar}[\hat{H}_{\text{S-F}}(t),\hat{\rho}(t)] + \sum_{P=L,M,R}\mathcal{L}_P[\hat{\rho}(t)]. \tag{12}$$

The Lindblad superoperator $\mathcal{L}_P[\hat{\rho}]$ quantifies the influence of the thermal bath B_P on the system S and is written

$$\begin{aligned}\mathcal{L}_P[\hat{\rho}] = \sum_{\omega>0}\Bigg(&\mathcal{J}_P(\omega)(1+n_P(\omega))\Bigg(\hat{A}_P(\omega)\hat{\rho}\hat{A}_P^\dagger(\omega)\\ &-\frac{1}{2}\{\hat{A}_P^\dagger(\omega)\hat{A}_P(\omega),\hat{\rho}\}\Bigg)+\mathcal{J}_P(\omega)n_P(\omega)\\ &\times\left(\hat{A}_P^\dagger(\omega)\hat{\rho}\hat{A}_P(\omega)-\frac{1}{2}\{\hat{A}_P(\omega)\hat{A}_P^\dagger(\omega),\hat{\rho}\}\right)\Bigg).\end{aligned} \tag{13}$$

where ω runs through all allowed positive energy transitions in the system. Here, $n_P(\omega)$ represents the population of the harmonic oscillator mode with frequency ω in B_P and is given by

$$n_P(\omega) = \frac{1}{\exp\left(\frac{\hbar\omega}{k_B T_P}\right)-1}. \tag{14}$$

Each bath B_P is hence characterized by its spectral function $\mathcal{J}_P(\omega)$ and its temperature T_P. For simplicity we consider all three reservoirs as having the same Ohmic spectral function $\mathcal{J}_P(\omega)=\kappa\omega$.

The Lindblad operator $\hat{A}_P(\omega)$ is associated with a transition of energy $\hbar\omega$ induced in S by thermal bath B_P and is given by

$$\hat{A}_P(\omega) = \sum_{\epsilon'-\epsilon=\hbar\omega}\hat{\Pi}(\epsilon)\hat{\sigma}_x^P\hat{\Pi}(\epsilon') \tag{15}$$

with $\hat{\Pi}(\epsilon)$ being the projection operator for $\hat{H}_S$ towards the system energy eigenvalue ϵ (see Appendix B). Upon further analysis, we find that most $\hat{A}_P(\omega)$ operators are zero, and that the twelve remaining nonzero operators all correspond to bath induced transitions shown in Fig. 2.

C. Conditions for model validity

At this point, we would like to briefly discuss the various approximations we had to perform while modeling our system and the corresponding conditions a physical system needs to satisfy in order to align with them.

As discussed in Appendix A, we had to perform the Born, Markov, and RWA approximations while deriving the quantum master equation given in Eq. (12). Under Born and Markov approximations, we respectively assume that the thermal reservoirs are minimally affected by the dynamics of the system, and that they are essentially memoryless within the time-scales we are considering [31,37]. The corresponding physical condition for these is that the thermal reservoirs B_P are large enough to supply the heat flows J_P to the system without their temperature or other thermal properties being significantly affected.

Under RWA we assume that the timescale τ_S associated with the energy levels of the system is much smaller than the timescale τ_R associated with the thermal relaxation of the system [31,37]. We can easily approximate τ_S by finding typical values of $2\pi\hbar/(\epsilon_i-\epsilon_j)$ for $i\neq j$. However, to find τ_R we have to first solve Eq. (12) for different initial conditions and parameter sets, obtain the time evolution of the system density matrix $\hat{\rho}(t)$ for each case, and then approximate the time taken by the system to reach its stationary condition. We subsequently have to check the condition $\tau_R \gg \tau_S$ to verify the validity of RWA for our model.

Since our model has multiple thermal reservoirs, we naturally have to ensure that direct thermal flows between the reservoirs, except across our system, are physically inhibited. Similarly, the thermal reservoirs should be shielded from the external optical field to prevent direct optothermal interactions between them.

D. Thermal energy flows

Conservation of energy with respect to the system S leads us to the following continuity equation [24]:

$$\begin{aligned} J_F(t) + \sum_{P=L,M,R} J_P(t) &= \frac{\partial \langle \hat{H}_S \rangle}{\partial t} \\ &= \frac{\partial}{\partial t} \mathrm{Tr}\{\hat{H}_S \hat{\rho}(t)\} \\ &= \mathrm{Tr}\left\{ \hat{H}_S \frac{d\hat{\rho}(t)}{dt} \right\}, \end{aligned} \tag{16}$$

where $\mathrm{Tr}\{\hat{A}\} = \sum_{j=1}^{8} \langle j|\hat{A}|j\rangle$ is the matrix trace. Substituting from Eq. (12)

$$\begin{aligned} J_F(t) + \sum_{P=L,M,R} J_P(t) =& \mathrm{Tr}\left\{ -\frac{i}{\hbar} \hat{H}_S [\hat{H}_{\text{S-F}}(t), \hat{\rho}(t)] \right\} \\ &+ \sum_{P=L,M,R} \mathrm{Tr}\{\hat{H}_S \mathcal{L}_P[\hat{\rho}(t)]\} \end{aligned} \tag{17}$$

and comparing similar terms, we conclude

$$J_F(t) = \mathrm{Tr}\left\{ -\frac{i}{\hbar} \hat{H}_S [\hat{H}_{\text{S-F}}(t), \hat{\rho}(t)] \right\} \tag{18}$$

$$J_P(t) = \mathrm{Tr}\{\hat{H}_S \mathcal{L}_P[\hat{\rho}(t)]\}. \tag{19}$$

Following the procedure in Appendix B, we derive the following expressions for the energy inflows into S:

$$\begin{aligned} J_F &= -(\epsilon_{24}\Upsilon_{24} + \epsilon_{57}\Upsilon_{57}), \\ J_L &= -\left(\epsilon_{51}\Gamma^L_{51} + \epsilon_{62}\Gamma^L_{62} + \epsilon_{73}\Gamma^L_{73} + \epsilon_{84}\Gamma^L_{84}\right), \\ J_M &= -\left(\epsilon_{31}\Gamma^M_{31} + \epsilon_{42}\Gamma^M_{42} + \epsilon_{75}\Gamma^M_{75} + \epsilon_{86}\Gamma^M_{86}\right), \\ J_R &= -\left(\epsilon_{21}\Gamma^R_{21} + \epsilon_{43}\Gamma^R_{43} + \epsilon_{65}\Gamma^R_{65} + \epsilon_{87}\Gamma^R_{87}\right), \end{aligned} \tag{20}$$

where $\epsilon_{jk} = \epsilon_j - \epsilon_k$ is the energy released in a single transition from $|j\rangle$ to $|k\rangle$,

$$\Gamma^P_{jk} = \mathcal{J}_P(\omega_{jk})((1 + n_P(\omega_{jk}))\rho_{jj} - n_P(\omega_{jk})\rho_{kk}) \tag{21}$$

is the net transition rate from $|j\rangle$ to $|k\rangle$ induced by the interaction of the system S with reservoir B_P, and

$$\Upsilon_{jk} = i\frac{\Omega}{2}(\rho_{jk} - \rho_{kj}) \tag{22}$$

is the net transition rate from $|j\rangle$ to $|k\rangle$ induced by the interaction of the system S with the field F. Here, $\omega_{jk} = \epsilon_{jk}/\hbar$, ρ_{jk}s represent the matrix elements of the density matrix $\hat{\rho}$, and for clarity we have dropped the explicit time dependence. From observing Eq. (20) and Fig. 2, we clearly see that each term in the energy flows corresponds to a transition in the system induced by that particular external entity.

III. CALCULATING SYSTEM DYNAMICS

Fully expanding Eq. (12) will provide a system of 64 first order differential equations of motion, one for each density matrix element. Given the initial state $\hat{\rho}(0)$, the system can then be solved to obtain the time evolution of S, after which we can use Eq. (20) to calculate the energy flows.

When solving Eq. (12) we find that most density matrix elements ρ_{jk} exponentially decays to zero, regardless of the initial state. In the long term, the only nonzero terms happen to be the diagonal elements ρ_{jj}, and the off-diagonal elements ρ_{24}, ρ_{42}, ρ_{57} and ρ_{75}. The equations of motion for the diagonal density matrix elements are given by

$$\begin{aligned} \dot{\rho}_{11} &= +\Gamma^L_{51} + \Gamma^M_{31} + \Gamma^R_{21}, \\ \dot{\rho}_{22} &= +\Gamma^L_{62} + \Gamma^M_{42} - \Gamma^R_{21} - \Upsilon_{24}, \\ \dot{\rho}_{33} &= +\Gamma^L_{73} - \Gamma^M_{31} + \Gamma^R_{43}, \\ \dot{\rho}_{44} &= +\Gamma^L_{84} - \Gamma^M_{42} - \Gamma^R_{43} + \Upsilon_{24}, \\ \dot{\rho}_{55} &= -\Gamma^L_{51} + \Gamma^M_{75} + \Gamma^R_{65} - \Upsilon_{57}, \\ \dot{\rho}_{66} &= -\Gamma^L_{62} + \Gamma^M_{86} - \Gamma^R_{65}, \\ \dot{\rho}_{77} &= -\Gamma^L_{73} - \Gamma^M_{75} + \Gamma^R_{87} + \Upsilon_{57}, \\ \dot{\rho}_{88} &= -\Gamma^L_{84} - \Gamma^M_{86} - \Gamma^R_{87}, \end{aligned} \tag{23}$$

and equations of motion for the nonzero off-diagonal elements are given by

$$\begin{aligned} \dot{\rho}_{24} &= \gamma_{42} - \tfrac{1}{2}\left(\beta^L_{62} + \beta^L_{84} + \alpha^M_{42} + \beta^M_{42} + \alpha^R_{21} + \alpha^R_{43}\right)\rho_{24}, \\ \dot{\rho}_{42} &= \gamma_{24} - \tfrac{1}{2}\left(\beta^L_{62} + \beta^L_{84} + \alpha^M_{42} + \beta^M_{42} + \alpha^R_{21} + \alpha^R_{43}\right)\rho_{42}, \\ \dot{\rho}_{57} &= \gamma_{75} - \tfrac{1}{2}\left(\alpha^L_{51} + \alpha^L_{73} + \alpha^M_{75} + \beta^M_{75} + \beta^R_{65} + \beta^R_{87}\right)\rho_{57}, \\ \dot{\rho}_{75} &= \gamma_{57} - \tfrac{1}{2}\left(\alpha^L_{51} + \alpha^L_{73} + \alpha^M_{75} + \beta^M_{75} + \beta^R_{65} + \beta^R_{87}\right)\rho_{75}, \end{aligned} \tag{24}$$

where $\alpha^P_{jk} = \mathcal{J}(\omega_{jk})(1 + n_P(\omega_{jk}))$, $\beta^P_{jk} = \mathcal{J}(\omega_{jk})n_P(\omega_{jk})$, and $\gamma_{jk} = i\frac{\Omega}{2}(\rho_{jj} - \rho_{kk})$. Note how each off-diagonal equation has a γ_{jk} term which is proportional to the Rabi frequency Ω and therefore, to the optical field amplitude $|\vec{E}_0|$. This term originates from the field interaction $\hat{H}_{\text{S-F}}(t)$ in Eq. (8) which couples together the states $|2\rangle \leftrightarrow |4\rangle$ and $|5\rangle \leftrightarrow |7\rangle$. Without this extra term, the solutions of Eq. (24) would all exponentially decay to zero. Incidentally, the absence of the γ_{jk} coupling term in the equations of motion of the other off-diagonal elements is the exact reason why they all eventually decay to zero.

From analyzing Eqs. (23) and (24), it can be shown that stationary solutions do exist for the density matrix, and that the system eventually stabilizes to that solution from any initial state. This existence of stationary solutions originates from the RWA approximation we carried out when deriving Eq. (8). Alternatively, converting Eq. (6) into the interaction picture without RWA will result in a significantly more complicated system of differential equations, whose solutions will generally not converge to stationary values. However, we found by simulating both formalisms that the thermal gating behaviors we are interested in shows up regardless of whether RWA is used or not. Therefore we have chosen to present the model with RWA here due to its comparative simplicity.

In this work, we are mainly investigating the long-term thermal conductivity through S, once the amplitude of the optical field and the bath temperatures have been fixed at certain values for a while. We are less interested in what happens while the bath temperatures and field amplitudes themselves are changing dynamically. In other words, we seek the heat flows through S once the transient effects due to the initial conditions have died out and the quantum state

of the system settles to its steady state. We can obtain this condition by searching for solutions of Eqs. (23) and (24) while asserting $\frac{d\hat{\rho}}{dt} = 0$.

We will not present the closed form solutions of Eqs. (23) and (24) here due to space considerations. Rather, we opt to present only the results and conclusions obtained by numerically simulating our device for a wide range of system, field and environment parameters. For the interested reader, the full MATHEMATICA codes for the simulations are available in Ref. [38].

IV. SIMULATIONS AND RESULTS

In this section, we present the results we obtained by numerically simulating the behaviors of our quantum system for different sets of system, optical field and environment parameters. Note that in the following, we work in SI units where $\hbar = 1.055 \times 10^{-34}$ J s and $k_B = 1.381 \times 10^{-23}$ J/K.

A. Simulation parameters

We prepare the thermal reservoirs B_L and B_R so that the temperature T_L of B_L is significantly higher than the temperature T_R of B_R. The thermodynamic tendency of S would then be to conduct heat from hot reservoir B_L to cold reservoir B_R. However, the actual amount of heat flow would depend on the thermal properties of S.

Joulain *et al.* [26] previously analysed this system for the special case when the field F was absent. They discovered that for certain system parameters the heat flow between B_L and B_R could be effectively controlled by adjusting the temperature T_M of bath B_M between the minimum value T_R and the maximum value T_L. They additionally discovered that during this controlling action, the heat flow J_M through the control reservoir B_M remained significantly smaller than the heat flows J_L and J_R it regulated. In summary, they discovered that the system operated analogous to an electronic FET, with temperatures acting as voltages, heat flows as currents, B_L and B_R as source and drain terminals, and B_M as the gate terminal.

Since in this work we plan to move the control terminal from B_M to F, we have to fix T_M to some constant value beforehand. In our simulations, we set $T_M = T_R$ to bias the transistor to its fully insulating setting, so that it blocks heat flow between B_L and B_R as much as possible in the absence of F. This bias has the additional advantage of being easy to realize practically since the reservoirs B_M and B_R have the same temperature.

Our next task is to select the appropriate system parameters. For proper operation, the overall scale of the system energy levels should be chosen to be around five times greater than the energy levels associated with the thermal baths [26]. Mathematically, this condition can be written as

$$\hbar\omega \approx 5k_BT, \tag{25}$$

where ω and T represent the typical frequency and the temperature scales associated with the system and its environment. We then specify the relationships between different energy levels as $\omega_L = \omega_R = 0$, $\omega_{RL} = 0$, and $\omega_{LM} = \omega_{MR} \gg \omega_M > 0$ to obtain a system whose energy level diagram is similar to Fig. 2. This provides us with a relatively simple system while showcasing thermal gating behavior well.

The condition $\omega_{RL} = 0$ makes sure that thermal flows through the system are always mediated through TLS M, and must be satisfied at least approximately for proper thermal gating operation. The condition $\omega_{LM} = \omega_{MR}$ is necessary to preserve the form of $\hat{H}_{\text{S-F}}$ in Eq. (6) by making sure both field-induced transitions are exactly resonant. This has the additional effect of making the energy eigenstate pairs $|\uparrow\uparrow\downarrow\rangle - |\downarrow\uparrow\uparrow\rangle$ and $|\downarrow\downarrow\uparrow\rangle - |\uparrow\downarrow\downarrow\rangle$ degenerate. It makes the system symmetrical with respect to the thermal baths B_L and B_R, and simplifies the mathematics considerably.

However, it is important to note here that, further simulations have shown that the condition $\omega_{LM} = \omega_{MR}$ is not strictly necessary for demonstrating thermal gating behavior. As we shall see in Sec. V, only the optically induced $|\downarrow\downarrow\uparrow\rangle$ to $|\downarrow\uparrow\uparrow\rangle$ transition, which absorbs energy from F, is critical for thermal gating when $T_L > T_R$. As long as the field is chosen to be resonant with that particular transition, changing the field amplitude will regulate the heat flow between B_L and B_R, even if the other transition $|\uparrow\uparrow\downarrow\rangle \leftrightarrow |\uparrow\downarrow\downarrow\rangle$ is off-resonant. Conversely, the transition $|\uparrow\uparrow\downarrow\rangle \leftrightarrow |\uparrow\downarrow\downarrow\rangle$ will become critical if we interchange the thermal baths so that $T_L < T_R$. In this paper, we have chosen to include both transitions in our model for completeness and clarity.

In accordance with the above discussion, we select the temperatures for our simulations as $T_L = 300$ K and $T_M = T_R = 30$ K. Note that we have set the ratio to 10 between the high to low temperatures to mirror corresponding values used in Ref. [26]. This allows us to perform a fair comparison between the two systems in the next section. However, our simulations have confirmed that thermal gating behaviors can be observed even for higher values of T_M and T_R (see Ref. [38]).

Using Eq. (25), we derive that the frequency scales in the system need to be around $\Delta = 3.12 \times 10^{13}$ Hz. Accordingly, we set the system parameters as $\omega_{LM} = \omega_{MR} = \Delta$ and $\omega_M = 0.1\Delta$. We further find that, to strongly drive the optical gating action, we require the Rabi frequencies to be in the low terahertz range, which is typical for optical driving applications similar to ours [39–41]. The frequency of the external optical field is calculated to be $\omega_F = 3.12 \times 10^{12}$ Hz, which puts it in the infrared spectrum.

B. Simulation results

We now simulate the steady-state conditions of our system for different Rabi frequencies Ω (and hence optical field amplitudes $|\vec{E}_0|$), and observe its effects on the system-bath and system-field energy flows.

The solid lines in Fig. 3 show the energy flows J_L, J_M, J_R, and J_F observed when continuously increasing the Rabi frequency Ω, starting from the case $\Omega = 0$ when the optical field is absent. In Fig. 4, we explore how sensitive these heat flows are to small changes in the optical field amplitude by plotting the field-sensitivity measures $\eta_P(\Omega)$ defined by

$$\eta_P(\Omega) = \frac{dJ_P(\Omega)}{d\Omega} \tag{26}$$

for $P = \{L, M, R, F\}$.

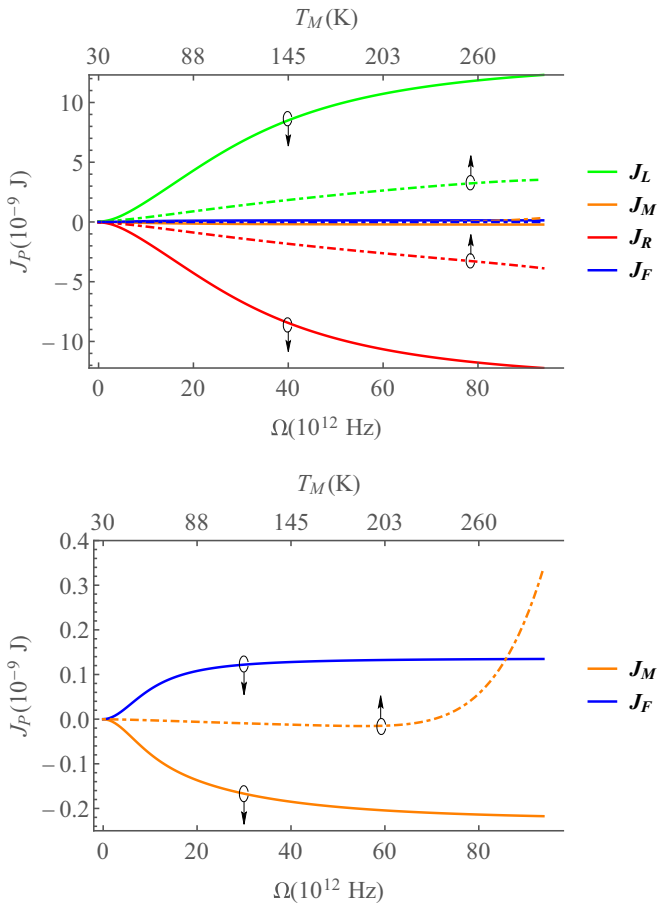

FIG. 3. (Solid) Total energy inflows at the steady state of our optical-gate system simulated for the Rabi frequency range $\Omega = [0, 3\Delta]$ with system parameters $\omega_L = \omega_R = \omega_{RL} = 0$, $\omega_{LM} = \omega_{MR} = \Delta$, $\omega_M = 0.1\Delta$, and environment parameters $T_L = 300$ K and $T_M = T_R = 30$ K. (Dashed) For comparison, the corresponding energy inflows of the thermal transistor system reported in Ref. [26] simulated for the temperature range $T_M = [30$ K, 300 K] with the same system and environment parameters. The direction of the arrows on each graph indicates the horizontal axis it corresponds to.

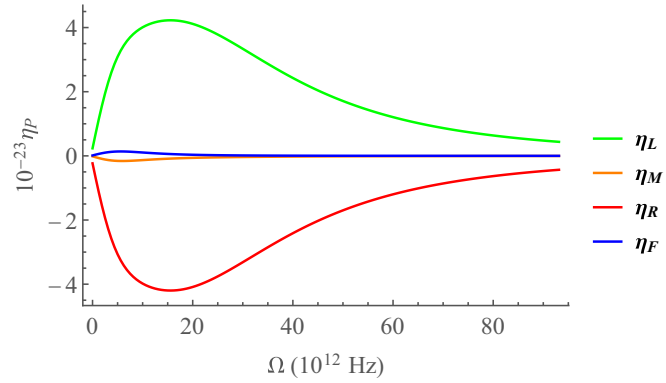

FIG. 4. Sensitivity of heat flows in our optical-gate system to changes in Rabi frequency, simulated with the same parameters as that of Fig. 3.

When the optical field is absent, or very weak, we observe from Fig. 3 that the system S only allows a minuscule heat flow between B_L and B_R, even though the temperature difference between them is considerable. This is in keeping with the choice we made when choosing the bias temperature T_M previously. We further observe that we can increase the heat flow to larger values as required, by appropriately increasing the Rabi frequency Ω. However, as we keep increasing Ω we find that the thermal conductivity of S eventually saturates and becomes less and less sensitive to further increases of optical field amplitude. From Fig. 4, we see in more detail how the sensitivity of the heat flows reaches a maximum for medium values of Rabi frequency, and falls off as Ω increases or decreases beyond that region. We will discuss the reasons for these behaviors further in Sec. V.

The energy efficiency of the above gating action can be quantified by the amplification ratio J_L/J_F, which measures the thermal energy flow controlled by the device in comparison to the amount of optical energy absorbed in doing so. We present this efficiency measure by the solid line in Fig. 5, from which we see that J_F is one to two orders of magnitude smaller than J_L for all simulated field parameters. This basically means that the device is very energy efficient, in that it absorbs only a small amount of energy from F even when regulating significantly larger heat flows between B_L and B_R.

We can observe from Fig. 3 that J_M is significantly smaller than both J_L and J_R for these parameters. This allows us to consider only J_L and J_R as important when analyzing how the Rabi frequency Ω of the optical field affects the system. Thereby we can get a simplified model for our system as a device whose thermal conductivity between two of its thermal terminals is controlled by the optical field imposed on its third optical terminal. However, it must be stressed that B_M is still an essential component for the proper operation of our device since it sets the base heat flow over which the

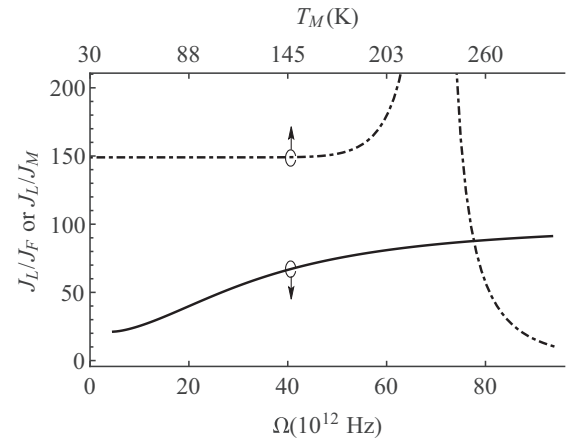

FIG. 5. (Solid) Ratio between the regulated thermal flow J_L and optical-field energy absorption J_F of our optical-gate system simulated for the Rabi frequency range $\Omega = [0, 3\Delta]$. (Dashed) For comparison, the corresponding energy inflows of the thermal transistor system reported in Ref. [26] simulated for the temperature range $T_M = [30$ K, 300 K]. The simulation parameters for both systems are the same as that of Fig. 3. The direction of the arrows on each graph indicates the horizontal axis it corresponds to.

optically induced flows build upon, and since it ensures that the local temperature of the terminal M does not drift during its operation.

Additional time-domain simulations (see Ref. [38]) have shown that relaxation times τ_R for our simulated system are generally around 5×10^{-11} s when $\Omega = 0$, and reduces to around 5×10^{-12} s when $\Omega = 3\Delta$. For the same parameter set, the maximum value of τ_S can be calculated to be around $2\pi/\omega_M = 3 \times 10^{-13}$ s by considering the smallest energy transitions $|\downarrow\downarrow\uparrow\rangle \leftrightarrow |\downarrow\uparrow\uparrow\rangle$ and $|\uparrow\uparrow\downarrow\rangle \leftrightarrow |\uparrow\downarrow\downarrow\rangle$. We observe from these values that τ_R is always over an order of magnitude larger than τ_S for the Ω range we consider, verifying the validity of our initial approximations.

In summary, these results show that our system regulates the heat flow $J_L \approx J_R$ between thermal baths B_L and B_R in response to the amplitude of the radiation field F, while absorbing a significantly smaller amount of energy from F. We can clearly see that our system is capable of acting as an energy efficient optically controlled thermal gating device.

C. Comparison with temperature based control

In this section, we briefly compare the performance of our optically controlled thermal gate with the temperature-controlled thermal transistor reported in Ref. [26].

The control parameter of the previous device was the temperature T_M, which was adjustable within the range $[T_R, T_L]$. In the new device, we have moved the control parameter to the Rabi frequency Ω, which corresponds to the driving strength of the external optical field. The controllable range of Ω has a lower bound of zero, but does not have a hard upper bound. However from Fig. 3 we can see that for large Ω values the heat flow eventually saturates, and increasing Ω beyond this point provides no advantage. We can use this saturation behavior to obtain an approximate upper bound for Ω, which turns out to be around 3Δ for our simulation parameters. Hence, we define the approximate control-parameter range of our device to be $[0, 3\Delta]$.

We can now compare the energy flows and amplification factors of these two devices by varying the control-parameter of each device within its corresponding range. We demonstrate our results in Figs. 3 and 5, where we have used solid lines to represent the values from our system, and dashed lines to represent the values reproduced from the device of Joulain *et al.* [26] for the same parameter set.

From Fig. 3, we observe that within their respective control-parameter ranges, the controlled thermal flows J_L and J_R of our device are several times larger than those of the previous device. While the heat flows of the previous system could be enhanced further by raising T_M beyond T_L, we note that this would also exponentially increase J_M to the point that the system no longer performs as a transistor. We hence conclude that, compared to the previous system, our system can control heat flows over a significantly larger range.

By observing values for J_F and J_M in Fig. 3, we find that the energy absorbed from the optical field F in our system is significantly higher than the energy absorbed from the control-bath B_M in the previous system. In other words, even though our device controls comparatively larger heat flows, it also consumes a larger amount of energy while doing so. To investigate what this means for the energy efficiency of these two devices, we plot their energy amplification factors J_L/J_F and J_L/J_M in Fig. 5. We observe that the increased energy consumption of our device has made it generally less energy efficient than the previous temperature-controlled device. We further observe that the behavior of the amplification factors in response to their respective control parameters is quite different in these two devices.

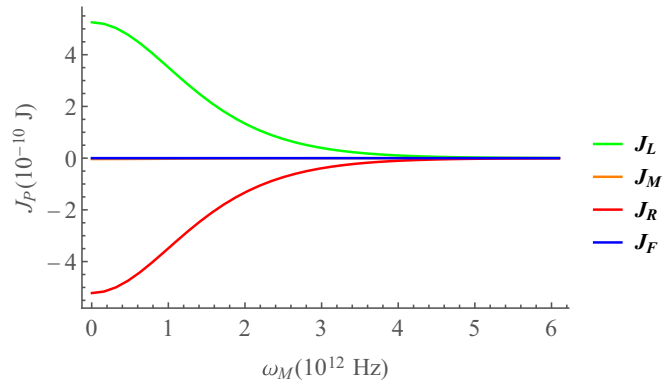

FIG. 6. Leakage heat flows (i.e., flows at $\Omega = 0$) of the optical gating system while varying ω_M within the range $[0, 0.2\Delta]$. All other system and environment parameters are the same as that of Fig. 3.

From our results, we conclude that our device is favoured in situations where the superior controllable range of heat flows is more important than the reduction in energy efficiency. However, we stress that the main contribution of this work is to shift the control terminal of the device from the thermal bath B_M to the optical field F. The easier localization and control of optical fields in the nanoscale would make our device useful in a wider range of applications than the original temperature-controlled device.

D. Effect of system parameters on heat flows

Simulations have shown that different ω_P and ω_{PQ} parameters allow for widely different gating behaviors and performance measures such as saturation heat flow, leakage heat flow, efficiency, field sensitivity, etc. Hence tuning these parameters allow us to optimize our device for different usage requirements, just like for an electronic transistor. We consider a detailed discussion of such optimization beyond the scope of this paper.

However, for completeness, we will briefly discuss in this section the effects of changing the two nonzero parameters ω_M and $\omega_{LM} = \omega_{MR}$ of the simplified system we simulated previously. We will specifically concentrate on how these parameters affect the leakage and saturation heat flows through the system. We define leakage and saturation heat flows as the amount of heat conducted when the system is at its fully insulating setting (when $\Omega = 0$) and its fully conducting setting (when $\Omega \approx 3\Delta$), respectively.

From Fig. 6, we observe that increasing ω_M causes a significant decrease in the leakage current flows in the system. However, since we have to set $\omega_F = \omega_M$ for resonance, this also means that we have to use a higher frequency optical field. This subsequently increases the energy absorption from

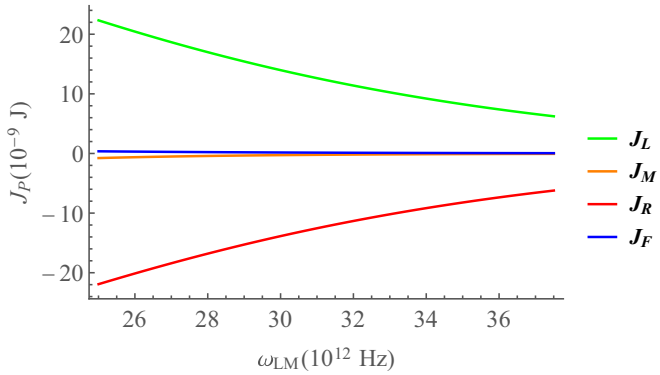

FIG. 7. Saturation heat flows (i.e., flows at $\Omega = 3\Delta$) of the optical gating system while varying $\omega_{LM} = \omega_{MR}$ within the range $[0.8\Delta, 1.2\Delta]$. All other system and environment parameters are the same as that of Fig. 3.

the optical field J_F for $0 < \Omega < 3\Delta$, leading to a degradation of the energy efficiency of the system. Further simulations have shown that increasing ω_M does not significantly change the saturation heat flows J_L and J_R of the system.

On the other hand, increasing $\omega_{LM} = \omega_{MR}$ has a similar negative effect on all the heat flows of the system for all values of Ω. We present the effect of ω_{LM} on the saturation heat flows in Fig. 7. The effect on the leakage heat flows follow a similar profile, albeit at lower overall magnitudes. Since all heat flows in the system are affected similarly, the device energy efficiency is not significantly affected.

The causal relationships between these parameters and the thermal properties of the device will become clearer in the following section when we discuss the underlying operating principles of our device.

V. MECHANISM OF OPERATION

In the previous section, we have demonstrated through numerical simulations the thermal gating behaviors of our device. In this section, we illustrate its mechanism of operation and discuss how it could be manipulated to suit different performance parameters. For this, we primarily use the diagrams in Figs. 8 and 9 as visual aids.

A. State and transition rate diagrams

We use the state diagrams in Fig. 8 to present the steady-state situation of S in a compact and intuitive manner. Each diagram fully describes the state population densities, energy levels, transition rates, and heat flows at the steady-state condition for a given set of parameters.

The eight system eigenstates $|j\rangle$ are ordered in the vertical axis according to their energy eigenvalues. The area of each blue eigenstate marker is proportional to its corresponding density matrix element ρ_{jj} (and therefore its population density at the steady-state condition).

By observing Eq. (23), we see that field-induced transition rate Υ_{jk} and bath-induced transition rate Γ^P_{jk} both correspond to a flow of population density from eigenstate $|j\rangle$ to eigenstate $|k\rangle$. We represent these transition rates in our diagrams by arrows between their corresponding start-state and end-state

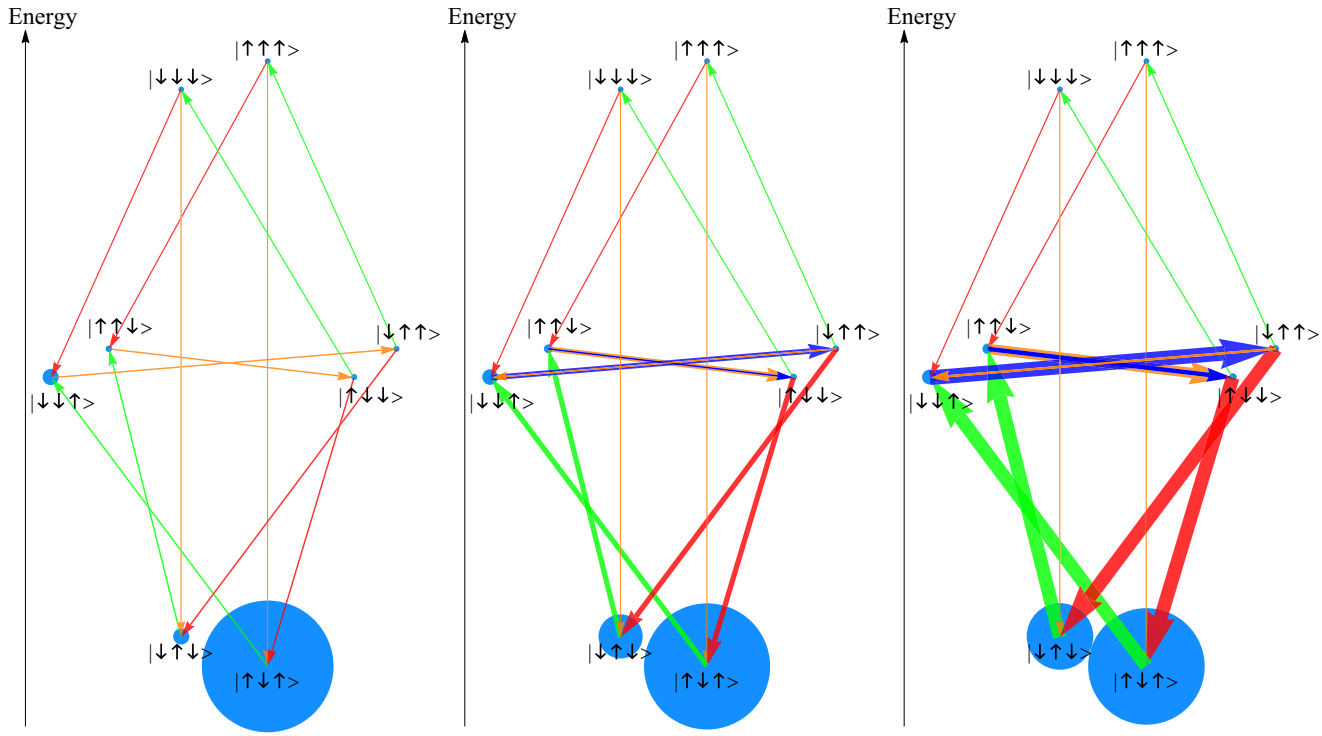

FIG. 8. Numerically simulated state and transition rate diagrams of the system S at the steady state for different Rabi frequencies Ω. For all three cases shown, $\omega_L = \omega_R = \omega_{RL} = 0$, $\omega_{LM} = \omega_{MR} = \Delta$, $\omega_M = 0.1\Delta$, $\omega_F = \omega_M + \omega_{LM} - \omega_{MR}$, $T_L = 300$ K, and $T_M = T_R = 30$ K.

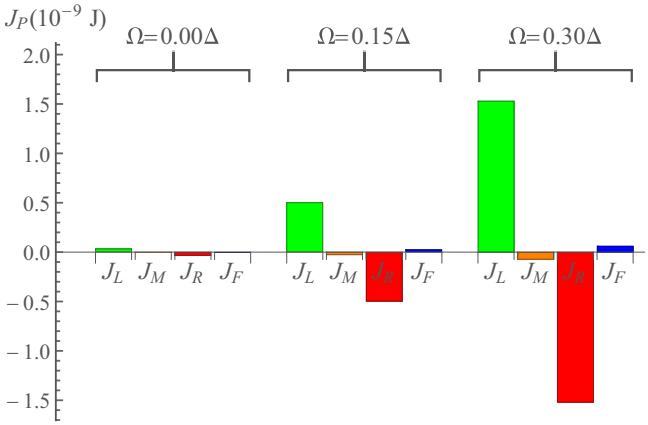

FIG. 9. Total energy inflows J_L, J_M, J_R, and J_F to the system S for the situations in Fig. 8. Increasing Ω significantly increases J_L and J_R, while keeping J_M and J_F at a comparatively lower level.

nodes. Green, orange, red, and blue arrows correspond to transitions induced by B_L, B_M, B_R, and F respectively. Arrow thickness is proportional to the magnitude of the transition rate, while arrow direction represents the direction of population density flow. The steady-state condition, which says that the population densities are time-invariant, is represented in the diagram by the flows to and from each eigenstate node summing to zero.

From Eq. (20) we see that each transition rate is associated with an energy absorption/emission from S to B_L, B_M, B_R, or F. Accordingly, an upward arrow in Fig. 8 indicates that S absorbs energy from the field/bath corresponding to its color. A downward arrow similarly indicates an emission of energy. The length of the arrow in the vertical axis represents the amount of energy absorbed/emitted per unit transition rate. This means that the energy flows from each external field/bath can be directly read from the diagram by observing the thicknesses, vertical lengths and directions of all the arrows with the appropriate color. However, we have separately calculated and graphed them in Fig. 9 for clarity.

B. Effect of bath interactions on the system

From the definition for Γ^P_{jk} in Eq. (21), we observe that the bath-induced transition rate from $|j\rangle$ to $|k\rangle$ is a complicated function of the bath temperature T_P, the transition energy difference $\hbar\omega_{jk}$, and state population densities ρ_{jj} and ρ_{kk}. For a given T_P and ω_{jk}, we find that the transition rate becomes zero only when the population densities satisfy

$$\frac{\rho_{jj}}{\rho_{kk}} = \frac{n_P(\omega_{jk})}{1 + n_P(\omega_{jk})}. \tag{27}$$

If the population densities deviate from this ratio, we find that Γ^P_{jk} generates an opposing flow between $|j\rangle$ and $|k\rangle$ in a manner to restore the population densities back to its original ratio. The steady-state condition of multibath quantum systems such as S arises from the complex interplay between the different thermal baths trying to balance the state populations to suit their own ratios.

However, some very simple rules of thumb can be extracted from observing Eq. (21), which can then be used to analyze any complicated system. Firstly, for a given $\omega_{jk} > 0$, Eq. (27) implies $\rho_{jj} = \rho_{kk}$ for very large T_P, and $\rho_{jj} \ll \rho_{kk}$ for very small T_P. Secondly, for a given T_P, Eq. (27) implies $\rho_{jj} = \rho_{kk}$ for very small ω_{jk}, and $\rho_{jj} \ll \rho_{kk}$ for very large positive ω_{jk}.

From the first observation, we conclude that high temperature baths tend to equalize the populations between the high-energy state $|j\rangle$ and low energy state $|k\rangle$, while low temperature baths tend to drive the system populations toward the low-energy state. From the second observation, we conclude that a bath with a given temperature better equalizes populations between states with similar energy levels, than between states with large energy differences. An immediate consequence is that increasing the temperature of the bath enhances its ability to equalize populations between larger energy differences.

We can now apply these rules for the system we simulate in Fig. 8, for which we have previously chosen the environment temperatures such that $T_L \gg T_M = T_R$. This choice of temperatures means that only the four transitions induced by the hot reservoir B_L (marked in green) can strongly drive populations in low-energy states towards higher energy states. During this process B_L has to feed energy into the system S.

In contrast, the four transitions induced by the cold reservoir B_R (marked in red) can only drive populations from high-energy states towards lower energy states, absorbing the excess energy from the system S. However, it can do so only if some other mechanism first generates a population in one of the high-energy states accessible to it (i.e., in states $|\downarrow\downarrow\downarrow\rangle$, $|\uparrow\uparrow\uparrow\rangle$, $|\uparrow\downarrow\downarrow\rangle$, or $|\downarrow\uparrow\uparrow\rangle$).

Since $T_M = T_R$ the capabilities of B_M is similar to that of B_R. However, the transitions induced by B_M and those of B_R are quite different. We see from Fig. 8 that while all four transitions associated with B_R have large energy differences, two of the four transitions associated with B_M (marked in orange) are quite short in the energy axis. The energy transition $|\downarrow\downarrow\uparrow\rangle \leftrightarrow |\downarrow\uparrow\uparrow\rangle$ in particular, is small enough that even with its low temperature B_M is capable of providing enough energy to sustain a tiny population flow from $|\downarrow\downarrow\uparrow\rangle$ to $|\downarrow\uparrow\uparrow\rangle$, provided the population in $|\downarrow\downarrow\uparrow\rangle$ is large enough compared to that of $|\downarrow\uparrow\uparrow\rangle$. As we shall see later, this transition is the critical part for generating the thermal gating behavior we require.

C. Effect of field interactions on the system

From the definition for Υ_{jk} in Eq. (22), we observe the expression for the field induced transition rate is dependent on the off-diagonal elements ρ_{jk} and ρ_{kj}. For the steady-state case, we can use Eq. (24) to replace the off-diagonal terms in Eq. (22) to obtain

$$\Upsilon_{jk} = \frac{\Omega^2}{\zeta_{jk}}(\rho_{jj} - \rho_{kk}), \tag{28}$$

where $\zeta_{24} = \zeta_{42} = \beta^L_{62} + \beta^L_{84} + \alpha^M_{42} + \beta^M_{42} + \alpha^R_{21} + \alpha^R_{43}$, $\zeta_{57} = \zeta_{75} = \alpha^L_{51} + \alpha^L_{73} + \alpha^M_{75} + \beta^M_{75} + \beta^R_{65} + \beta^R_{87}$, and $\Upsilon_{jk} = 0$ anyway for any other j and k.

By analyzing this expression we conclude that the tendency of the external field F is always to equalize the populations between its start and end states. The higher the amplitude $|\vec{E}_0|$ of the field, the greater the strength with which F tries

to equalize the populations. The temperatures of the thermal reservoirs also affect this interaction through ζ_{jk}, but we can ignore it for now because we are keeping the thermal baths constant while changing only Ω.

D. Mechanism of thermal conduction

We are now ready to analyze the state diagram in Fig. 8(a) which shows the equilibrium state of the system when the external field F is absent (i.e., $\Omega = 0$).

Since all three temperatures are finite, it is natural for the system S to mostly occupy the lowest energy level $|\uparrow\downarrow\uparrow\rangle$. The hot reservoir B_L can then establish a small population at $|\downarrow\downarrow\uparrow\rangle$ by providing to S the necessary energy to push out of the ground-state $|\uparrow\downarrow\uparrow\rangle$.

From $|\downarrow\downarrow\uparrow\rangle$ the system cannot take the red transition towards $|\downarrow\downarrow\downarrow\rangle$, since the bath B_R does not have a high enough temperature to provide the large amount of energy required. Therefore the only path from $|\downarrow\downarrow\uparrow\rangle$ we need to consider is the B_M induced transition towards $|\downarrow\uparrow\uparrow\rangle$. As discussed previously, B_M is capable of establishing a small population at $|\downarrow\uparrow\uparrow\rangle$ despite its low temperature since the transition is quite small in the energy axis. However, it is important to stress here that this transition is very weak because it involves absorbing energy from a low temperature reservoir.

Once the system is at $|\downarrow\uparrow\uparrow\rangle$, it has the option of either absorbing more energy from B_L to go up towards $|\uparrow\uparrow\uparrow\rangle$, or releasing the currently absorbed energy to B_R to go down towards $|\downarrow\uparrow\downarrow\rangle$. The natural tendency of S to gravitate towards low energy levels makes sure that the red transition towards $|\downarrow\uparrow\downarrow\rangle$ is almost always taken. In this way, the transition chain $|\uparrow\downarrow\uparrow\rangle \rightarrow |\downarrow\downarrow\uparrow\rangle \rightarrow |\downarrow\uparrow\uparrow\rangle \rightarrow |\downarrow\uparrow\downarrow\rangle$ drives a small population from the lowest energy level $|\uparrow\downarrow\uparrow\rangle$ to the second lowest energy level $|\downarrow\uparrow\downarrow\rangle$.

Using a similar approach, we can now trace another transition chain starting from $|\downarrow\uparrow\downarrow\rangle$, going through $|\uparrow\uparrow\downarrow\rangle$ and $|\uparrow\downarrow\downarrow\rangle$, to arrive again at the initial ground state $|\uparrow\downarrow\uparrow\rangle$. However, we see that the transitions induced by B_M and B_R in this second chain are both downwards (i.e., energy-releasing). Since the low temperature reservoirs B_L and B_R can readily drive such transitions, this means that all three transitions in the second transition chain are strongly driven.

By looking at the six element cycle of transitions described above from an energy perspective, we see that it provides the main mechanism of heat transport through S. The upward transitions $|\uparrow\downarrow\uparrow\rangle \rightarrow |\downarrow\downarrow\uparrow\rangle$ and $|\downarrow\uparrow\downarrow\rangle \rightarrow |\uparrow\uparrow\downarrow\rangle$ absorb thermal energy from B_L, while the transitions $|\uparrow\downarrow\downarrow\rangle \rightarrow |\uparrow\downarrow\uparrow\rangle$ and $|\downarrow\uparrow\uparrow\rangle \rightarrow |\downarrow\uparrow\downarrow\rangle$ release most of that energy to B_R. The other two transitions $|\downarrow\downarrow\uparrow\rangle \rightarrow |\downarrow\uparrow\uparrow\rangle$ and $|\uparrow\uparrow\downarrow\rangle \rightarrow |\uparrow\downarrow\downarrow\rangle$ induced by B_M are significantly smaller in the energy axis, and therefore exchanges only a small amount of energy.

We can calculate that when the system travels through this cycle once, an energy of $\epsilon_{73} + \epsilon_{26}$ is taken from B_L and an energy of $\epsilon_{56} + \epsilon_{43}$ is subsequently given to B_R, while the difference between the two is borne by B_M. We therefore see that the amount of power transported from B_L to B_R is determined by the transition rate of this cycle.

The effective transition rate of such a cycle is decided entirely by its weakest link, which we found in the previous discussion to be the B_M induced transition $|\downarrow\downarrow\uparrow\rangle \rightarrow |\downarrow\uparrow\uparrow\rangle$. The main reason for this weakness is that the temperature of the thermal bath B_M is not sufficient to provide even the small amount of power required to drive this transition. This stifles the energy flows in S for $\Omega = 0$ as seen in Fig. 9, and therefore we say that S acts as an insulator.

E. Thermal conduction enhancement

We demonstrated in the previous discussion that the heat conduction through S is limited by the relative weakness of the transition $|\downarrow\downarrow\uparrow\rangle \rightarrow |\downarrow\uparrow\uparrow\rangle$. In this section, we discuss the different ways we could enhance this transition and thereby improve the heat conductivity through S.

In Sec. V B, we demonstrated that raising the temperature of a bath enhances its tendency to equalize the start-state and end-state populations of each transition induced by it. Therefore, the most obvious way to enhance the $|\downarrow\downarrow\uparrow\rangle \rightarrow |\downarrow\uparrow\uparrow\rangle$ transition would be to increase the temperature T_M of the reservoir B_M. However, we also found that higher temperatures tend to make the baths drive higher energy transitions. This means that we must take care not to raise T_M high enough to affect the high-energy transitions $|\downarrow\uparrow\downarrow\rangle \leftrightarrow |\downarrow\downarrow\downarrow\rangle$ and $|\uparrow\downarrow\uparrow\rangle \leftrightarrow |\uparrow\uparrow\uparrow\rangle$.

The thermal transistor reported in Ref. [26] employs this mechanism to control the heat flows through J_L and J_R, by adjusting the temperature T_M appropriately within the $[T_R, T_L]$ range. Alternatively in this work, by introducing the optical field F we provide an additional mechanism which complements B_M's effort to drive the critical $|\downarrow\downarrow\uparrow\rangle \rightarrow |\downarrow\uparrow\uparrow\rangle$ transition.

In Sec. V C, we demonstrated that the tendency of the external field F is to equalize the populations of its end-states and that the strength of this effort depends on the Ω (and therefore, on the amplitude of the field). By observing Fig. 8(a), we see that the population of the lower energy state $|\downarrow\downarrow\uparrow\rangle$ is considerably greater than the population of the higher energy state $|\downarrow\uparrow\uparrow\rangle$. Therefore we can infer that introducing the field F and increasing its amplitude would generate and enhance a new transition rate Υ_{75} from $|\downarrow\downarrow\uparrow\rangle$ to $|\downarrow\uparrow\uparrow\rangle$. Similar to the thermal transistor case, this enhancement should correspondingly increase the energy flows J_L and J_R.

The simulations in Figs. 8(b) and 8(c), indeed verifies our hypothesis. Introducing F and increasing its amplitude considerably enhances all the transition rates of the six-element heat transport cycle. In Fig. 9, we see how the increased transition rates have caused a corresponding increase in the thermal energy flows. We also note that the equilibrium populations have changed considerably, owing to the enhanced transition rates. We further observe that the presence of F has shifted B_M from being an energy donor to its more natural state of being an energy receiver.

The eventual tapering off of the optical sensitivity of the system observed in Figs. 3 and 4 for high Rabi frequencies can be attributed to the optical field achieving its goal of equalizing the populations of $|\downarrow\downarrow\uparrow\rangle$ and $|\downarrow\uparrow\uparrow\rangle$. At low Ω values, when the two populations are still significantly different, increasing Ω correspondingly increases the ability of the field F to equalize them. In contrast, at high Ω values the field has already equalized the populations to a

large extent. Hence, further increases in Ω have diminished effect.

From $\hat{H}_{\text{S-F}}$, we derived in Eq. (8), we see that the transition between $|\uparrow\uparrow\downarrow\rangle$ and $|\uparrow\downarrow\downarrow\rangle$ is also driven by the field F. Yet from our simulations we see that this field-induced transition Υ_{24} is dwarfed by the bath-induced transition rate Γ^M_{24}. The presence of this additional transition does not effect the gating action in a major way. However, by releasing some of the absorbed energy back to the field it increases the energy efficiency of the device. Additionally, it makes the device symmetrical, so that it operates the same even if the temperatures T_L and T_R are interchanged.

We noted earlier in Fig. 3 that the controlled thermal flows in our optically controlled system are generally larger than those reported in Ref. [26]. This can be attributed to the completely different underlying mechanisms these two systems employ. In the previous device, the raised temperature T_M enhanced the transition rate Γ^M_{75} only indirectly via Eq. (14). Therefore it required a high temperature to properly equalize the two populations at $|\downarrow\downarrow\uparrow\rangle$ and $|\downarrow\uparrow\uparrow\rangle$. In contrast, our optical field was designed specifically to drive the Υ_{75} transition directly via Eq. (28), allowing it to equalize the two populations with greater efficacy.

As a concluding remark, we note that the relative positioning of the system eigenstates in the energy axis could be adjusted by changing the ω_P and ω_{PQ} parameters of S. Properly tuning these parameters will allow us to obtain different thermal gating behaviors from the system. For instance, reducing ω_M will correspondingly reduce the energy difference between the states $|\downarrow\downarrow\uparrow\rangle$ and $|\downarrow\uparrow\uparrow\rangle$. This will increase the ability of B_M to drive our critical transition even if the optical field is absent, leading to the increased leakage heat flows we saw in Fig. 6. On the other hand, reducing $\omega_{LM} = \omega_{MR}$ increases the initial population at state $|\downarrow\downarrow\uparrow\rangle$, which enhances both the field-induced transition Υ_{75} and bath-induced transition Γ^M_{75}. This again helps to enhance the heat flows through S as we saw in Fig. 7. As a final example, adjusting the ω_{PQ} parameters to break the degeneracy of $|\uparrow\uparrow\downarrow\rangle - |\downarrow\uparrow\uparrow\rangle$ and $|\downarrow\downarrow\uparrow\rangle - |\uparrow\downarrow\downarrow\rangle$ will allow us to choose ω_F so that only one of the transitions are driven by F. This will break the symmetry of the device with respect to B_L and B_R, which may be useful in certain applications. There are many other parameter changes we can perform on the system to adjust its behaviors. However, most such cases can be analysed and optimized in a simple manner, by following a similar approach to interpret the energy diagrams as we have done here.

VI. CONCLUSIONS

In this paper, we presented a quantum system made up of three interacting two-level systems placed in an environment consisting of a single-mode optical field and three thermal reservoirs. We modelled the interactions between the system and its environment within an open quantum systems framework. We thereby derived the expressions for the density matrices, transition rates, and energy flows for the steady-state condition of the system.

Our detailed theoretical analysis revealed that the thermal conductivity of the quantum system could be significantly altered by slightly varying the amplitude of the optical field incident upon it, and that the optical energy absorbed by the system in this process is over an order of magnitude smaller than the regulated heat flows. Using detailed numerical simulations, we further investigated the device operation for a wide range of material and system parameters. All these studies confirmed that the proposed device could function as an efficient thermal gating device within certain parameter ranges.

We subsequently illustrated the mechanism of operation of our gating device and developed graphical representations to help visualize the dynamics of the system. These diagrams were capable of intuitively and compactly representing the energy eigenstates, population densities, transition rates and energy flows in the steady-state of our quantum system. Along with several rules of thumb for qualitatively analyzing the effects of thermal baths and optical fields on the system, these diagrams allowed us to develop a simple procedure for analyzing and modifying our thermal gating device to fit different performance requirements.

We found that the graphical representations we developed are capable of representing the steady state of a wide range of different thermo-optical systems. We therefore believe the methods employed in this paper would be applicable for many other problems in quantum thermal science.

In summary, the main objectives of this paper were to expand the current models of quantum thermal devices to include optical interactions, to demonstrate that our specific quantum system shows optical gating behaviors, and to introduce simple, intuitive visual representations which could be used to understand and analyze complex quantum thermo-optical systems.

Finally, we remark on how the findings of this paper may be utilized towards creating materials with controllable thermal conductivity. We could envision a two-dimensional array of our quantum thermal gating devices, sandwiched between two graphene layers. The exceptional thermal conductivity of the graphene layers would ensure each individual gating device gets the proper temperature bias. A low-power laser with a properly chosen wavelength incident on the assembly would provide the external optical field for each device. Such an assembly could regulate the thermal energy flow between its two graphene layers in response to the amplitude of the laser field.

ACKNOWLEDGMENTS

R.T.W. would like to thank A. Devi and all members of AχL at Monash University including T. Perera and T. Warnakula for encouragement and insightful discussions. The work of R.T.W. is supported by the Monash University Institute of Graduate Research.

APPENDIX A: DERIVING THE QUANTUM MASTER EQUATION

The procedure for deriving the quantum master equation is quite similar to that followed in Chap. 3 of Breuer and Petruccione [31] for a single thermal bath case. Due to space limitations we will only present here the outline of the

derivation, concentrating mostly on the deviations arising from the presence of multiple baths and the external field.

We start from the interaction picture von Neumann equation

$$\frac{d\hat{\rho}_{\mathrm{T}}(t)}{dt} = -\frac{i}{\hbar}[\hat{H}_1(t), \hat{\rho}_{\mathrm{T}}(t)], \tag{A1}$$

where $\hat{\rho}_{\mathrm{T}}(t)$ is the interaction picture density matrix for the combined system and environment, and $\hat{H}_1$ is defined in Eq. (11). This differential equation has the formal solution

$$\hat{\rho}_{\mathrm{T}}(t) = \hat{\rho}_{\mathrm{T}}(0) - \frac{i}{\hbar}\int_0^t ds[\hat{H}_1(s), \hat{\rho}_{\mathrm{T}}(s)]. \tag{A2}$$

This equation describes the full dynamics of the system and its environment, while we are interested only in the dynamics of the system S. Therefore the unwanted dynamics of the thermal baths have to be averaged out by taking a partial trace through B_L, B_M and B_R. Substituting Eq. (A2) back in Eq. (A1) and taking the partial trace through the thermal baths yields

$$\frac{d\hat{\rho}(t)}{dt} = -\frac{i}{\hbar}[\hat{H}_{\text{S-F}}(t), \hat{\rho}(t)] - \frac{1}{\hbar^2}\mathrm{Tr}_{\mathrm{L,M,R}} \left\{\int_0^t ds\left[\sum_P \hat{H}^P_{\text{TLS-bath}}(t), [\hat{H}_1(s), \hat{\rho}_{\mathrm{T}}(s)]\right]\right\} \tag{A3}$$

where $\mathrm{Tr}_{\mathrm{L,M,R}}\{\hat{\rho}_T(t)\} = \hat{\rho}(t)$ and we have assumed without loss of generality that

$$\mathrm{Tr}_{\mathrm{L,M,R}}\left\{\left[\sum_P \hat{H}^P_{\text{TLS-bath}}(t), \hat{\rho}_{\mathrm{T}}(0)\right]\right\} = 0. \tag{A4}$$

We now perform the Born and Markov approximations to derive [36]

$$\frac{d\hat{\rho}(t)}{dt} = -\frac{i}{\hbar}[\hat{H}_{\text{S-F}}(t), \hat{\rho}(t)] - \frac{1}{\hbar^2}\mathrm{Tr}_{\mathrm{L,M,R}} \left\{\int_0^\infty ds\left[\sum_P \hat{H}^P_{\text{TLS-bath}}(t), \left[\sum_Q \hat{H}^Q_{\text{TLS-bath}}(t-s) + \hat{H}_{\text{S-F}}(t-s), \hat{\rho}(t)\otimes\hat{\rho}_L\otimes\hat{\rho}_M\otimes\hat{\rho}_R\right]\right]\right\}. \tag{A5}$$

To proceed, we require the explicit form of the interaction picture Hamiltonian $\hat{H}^P_{\text{TLS-bath}}(t)$ to substitute in Eq. (A5). Therefore we use Eqs. (3) and (15) to decompose $\hat{H}^P_{\text{TLS-bath}}(t)$ into eigenoperators of the system Hamiltonian $\hat{H}_S$,

$$\hat{H}^P_{\text{TLS-bath}}(t) = \sum_\omega e^{-i\omega t}\hat{A}_P(\omega)\otimes\hat{B}_P(t), \tag{A6}$$

where $\hat{B}_P(t) = \sum_k g_k(e^{-i\omega_k t}\hat{a}^P_k + e^{+i\omega_k t}\hat{a}^{P\dagger}_k)$. Additionally it is important to note that Eq. (A4) implies

$$\langle\hat{B}_P(t)\rangle = \mathrm{Tr}_{\mathrm{P}}\{\hat{B}_P(t)\hat{\rho}_P\} = 0. \tag{A7}$$

Next we prove the following relations:

$$\mathrm{Tr}_{\mathrm{L,M,R}}\left\{\left[\hat{H}^P_{\text{TLS-bath}}(t), [\hat{H}_{\text{S-F}}(t-s), \hat{\rho}(t)\otimes\hat{\rho}_L\otimes\hat{\rho}_M\otimes\hat{\rho}_R]\right]\right\} = 0, \tag{A8}$$

$$\mathrm{Tr}_{\mathrm{L,M,R}}\left\{\left[\hat{H}^P_{\text{TLS-bath}}(t), \left[\hat{H}^Q_{\text{TLS-bath}}(t-s), \hat{\rho}(t)\otimes\hat{\rho}_L\otimes\hat{\rho}_M\otimes\hat{\rho}_R\right]\right]\right\} = 0, \tag{A9}$$

for $P, Q = L, M, R$ and $P \neq Q$ by using Eq. (A6) to substitute for $\hat{H}^P_{\text{TLS-bath}}(t)$, then expanding both commutators, and finally using Eq. (A7). This allows us to significantly simplify Eq. (A5) and obtain

$$\frac{d\hat{\rho}(t)}{dt} = -\frac{i}{\hbar}[\hat{H}_{\text{S-F}}(t), \hat{\rho}(t)] - \frac{1}{\hbar^2}\sum_P \mathrm{Tr}_{\mathrm{L,M,R}} \left\{\int_0^\infty ds\left[\hat{H}^P_{\text{TLS-bath}}(t), \left[\hat{H}^P_{\text{TLS-bath}}(t-s), \hat{\rho}(t)\otimes\hat{\rho}_L\otimes\hat{\rho}_M\otimes\hat{\rho}_R\right]\right]\right\}. \tag{A10}$$

From observing Eq. (A10), we clearly see that the terms mixing two different thermal bath interactions, and the terms mixing the field interaction with thermal bath interactions have all become zero. We are left with a quantum master equation with four distinct terms, each term only concerned with a single external entity. This means that we can consider the system's interaction with each thermal bath independently from the other two thermal baths and the field.

Therefore obtaining Eq. (12) from Eq. (A10) is now a simple process of following the standard procedure for a single thermal reservoir (as discussed extensively in Ref. [31]) separately for B_L, B_M, and B_R. It is important to note that in this process we carry out two other major approximations. First, we perform RWA by neglecting the high frequency terms when simplifying the double commutators in Eq. (A10). Second, we assume the harmonic oscillators of bath P is thermally distributed, which means that its density matrix $\hat{\rho}_P$ is given by

$$\hat{\rho}_P = \frac{\exp\left[-\beta\hat{H}^P_{\text{bath}}\right]}{\mathrm{Tr}_{\mathrm{P}}\left\{\exp\left[-\beta\hat{H}^P_{\text{bath}}\right]\right\}}, \tag{A11}$$

where $\beta = \frac{1}{k_B T_P}$ is the thermodynamic beta. This second assumption is the eventual source of Eq. (14).

APPENDIX B: DERIVING ENERGY FLOWS AND LINDBLAD OPERATORS

The energy eigenvalue decomposition of Eq. (1) gives us an alternate form for the system Hamiltonian,

$$\hat{H}_S = \sum_{j=1}^{8}\epsilon_j|j\rangle\langle j|. \tag{B1}$$

The density matrix $\hat{\rho}(t)$ can be written in terms of its matrix elements as

$$\hat{\rho}(t) = \sum_{j=1}^{8}\sum_{k=1}^{8}\rho_{jk}|j\rangle\langle k|. \tag{B2}$$

We can directly obtain the expression for J_F in Eq. (20) by using above two definitions and Eq. (8) to substitute the terms in Eq. (18). However, obtaining expressions for bath energy flows J_P first requires evaluating the Lindblad superoperator $\mathcal{L}_P[\hat{\rho}]$.

The first step is to evaluate the projection operators $\hat{\Pi}(\epsilon)$ of $\hat{H}_S$, considering the energy degeneracies of $\hat{H}_S$. For instance,

if all energy eigenvalues are unique, we obtain

$$\hat{\Pi}(\epsilon) = \begin{cases} |j\rangle\langle j| & \text{if } \exists\ j \text{ s.t. } \epsilon = \epsilon_j \\ 0 & \text{otherwise.} \end{cases} \tag{B3}$$

Now Eq. (15) can be used to derive the Lindblad operators $\hat{A}_P(\omega)$ for the $\omega > 0$ case. For the unique eigenvalue case, we get 28 different possibilities for $\epsilon' - \epsilon$, requiring us to evaluate 28×3 Lindblad operators for the three reservoirs. However, doing so will show that only 12 among them are nonzero. We subsequently evaluate $\mathcal{L}_P[\hat{\rho}]$ in Eq. (13) for $P = L$, M, R, and substitute them in Eq. (19) to obtain the expressions for J_P in Eq. (20).

[1] B. M. Foley, M. Wallace, J. T. Gaskins, E. A. Paisley, R. L. Johnson-Wilke, J.-W. Kim, P. J. Ryan, S. Trolier-McKinstry, P. E. Hopkins, and J. F. Ihlefeld, Voltage-controlled bistable thermal conductivity in suspended ferroelectric thin-film membranes, ACS Appl. Mater. Interfaces **10**, 25493 (2018).

[2] I. Chowdhury, R. Prasher, K. Lofgreen, G. Chrysler, S. Narasimhan, R. Mahajan, D. Koester, R. Alley, and R. Venkatasubramanian, On-chip cooling by superlattice-based thin-film thermoelectrics, Nat. Nanotechnol. **4**, 235 (2009).

[3] G. Pernot, M. Stoffel, I. Savic, F. Pezzoli, P. Chen, G. Savelli, A. Jacquot, J. Schumann, U. Denker, I. Mönch *et al.*, Precise control of thermal conductivity at the nanoscale through individual phonon-scattering barriers, Nat. Mater. **9**, 491 (2010).

[4] A. Shakouri, Nanoscale thermal transport and microrefrigerators on a chip, Proc. IEEE **94**, 1613 (2006).

[5] J. Shin, J. Sung, M. Kang, X. Xie, B. Lee, K. M. Lee, T. J. White, C. Leal, N. R. Sottos, P. V. Braun *et al.*, Light-triggered thermal conductivity switching in azobenzene polymers, Proc. Natl. Acad. Sci. USA **116**, 5973 (2019).

[6] K. Pielichowska and K. Pielichowski, Phase change materials for thermal energy storage, Prog. Mater. Sci. **65**, 67 (2014).

[7] P. Shima, J. Philip, and B. Raj, Magnetically controllable nanofluid with tunable thermal conductivity and viscosity, Appl. Phys. Lett. **95**, 133112 (2009).

[8] A. P. Alivisatos, Semiconductor clusters, nanocrystals, and quantum dots, Science **271**, 933 (1996).

[9] D. Dzsotjan, A. S. Sørensen, and M. Fleischhauer, Quantum emitters coupled to surface plasmons of a nanowire: A green's function approach, Phys. Rev. B **82**, 075427 (2010).

[10] A. Delga, J. Feist, J. Bravo-Abad, and F. J. Garcia-Vidal, Quantum Emitters Near a Metal Nanoparticle: Strong Coupling and Quenching, Phys. Rev. Lett. **112**, 253601 (2014).

[11] F. Hetsch, N. Zhao, S. V. Kershaw, and A. L. Rogach, Quantum dot field effect transistors, Mater. Today **16**, 312 (2013).

[12] H. Gleiter, T. Schimmel, and H. Hahn, Nanostructured solids–from nano-glasses to quantum transistors, Nano Today **9**, 17 (2014).

[13] D. E. Chang, A. S. Sørensen, E. A. Demler, and M. D. Lukin, A single-photon transistor using nanoscale surface plasmons, Nat. Phys. **3**, 807 (2007).

[14] D. Tiarks, S. Baur, K. Schneider, S. Dürr, and G. Rempe, Single-Photon Transistor Using a Förster Resonance, Phys. Rev. Lett. **113**, 053602 (2014).

[15] H. Gorniaczyk, C. Tresp, J. Schmidt, H. Fedder, and S. Hofferberth, Single-Photon Transistor Mediated by Interstate Rydberg Interactions, Phys. Rev. Lett. **113**, 053601 (2014).

[16] S. Sun, H. Kim, Z. Luo, G. S. Solomon, and E. Waks, A single-photon switch and transistor enabled by a solid-state quantum memory, Science **361**, 57 (2018).

[17] M. Schmotz, J. Maier, E. Scheer, and P. Leiderer, A thermal diode using phonon rectification, New J. Phys. **13**, 113027 (2011).

[18] D. Hatanaka, I. Mahboob, K. Onomitsu, and H. Yamaguchi, A phonon transistor in an electromechanical resonator array, Appl. Phys. Lett. **102**, 213102 (2013).

[19] J.-H. Jiang, M. Kulkarni, D. Segal, and Y. Imry, Phonon thermoelectric transistors and rectifiers, Phys. Rev. B **92**, 045309 (2015).

[20] B. Liu, W. Zhu, S. D. Gunapala, M. I. Stockman, and M. Premaratne, Open resonator electric spaser, ACS Nano **11**, 12573 (2017).

[21] C. Jayasekara, M. Premaratne, S. D. Gunapala, and M. I. Stockman, Mos2 spaser, J. Appl. Phys. **119**, 133101 (2016).

[22] I. Aharonovich, D. Englund, and M. Toth, Solid-state single-photon emitters, Nat. Photonics **10**, 631 (2016).

[23] R. H. Hadfield, Single-photon detectors for optical quantum information applications, Nat. Photonics **3**, 696 (2009).

[24] T. Werlang, M. A. Marchiori, M. F. Cornelio, and D. Valente, Optimal rectification in the ultrastrong coupling regime, Phys. Rev. E **89**, 062109 (2014).

[25] D. Segal and A. Nitzan, Spin-Boson Thermal Rectifier, Phys. Rev. Lett. **94**, 034301 (2005).

[26] K. Joulain, J. Drevillon, Y. Ezzahri, and J. Ordonez-Miranda, Quantum Thermal Transistor, Phys. Rev. Lett. **116**, 200601 (2016).

[27] B.-q. Guo, T. Liu, and C.-s. Yu, Quantum thermal transistor based on qubit-qutrit coupling, Phys. Rev. E **98**, 022118 (2018).

[28] R. Sánchez, H. Thierschmann, and L. W. Molenkamp, All-thermal transistor based on stochastic switching, Phys. Rev. B **95**, 241401(R) (2017).

[29] Y. Zhang, X. Zhang, Z. Ye, G. Lin, and J. Chen, Three-terminal quantum-dot thermal management devices, Appl. Phys. Lett. **110**, 153501 (2017).

[30] Y. Dubi and M. Di Ventra, Colloquium: Heat flow and thermoelectricity in atomic and molecular junctions, Rev. Mod. Phys. **83**, 131 (2011).

[31] H.-P. Breuer *et al.*, *The theory of Open Quantum Systems* (Oxford University Press on Demand, 2002).

[32] A. Caldeira and A. J. Leggett, Quantum tunneling in a dissipative system, Annals of physics **149**, 374 (1983).

[33] A. J. Leggett, S. Chakravarty, A. T. Dorsey, M. P. Fisher, A. Garg, and W. Zwerger, Dynamics of the dissipative two-state system, Rev. Mod. Phys. **59**, 1 (1987).

[34] M. Premaratne and G. P. Agrawal, *Light Propagation in Gain Media: Optical Amplifiers* (Cambridge University Press, 2011).

[35] M. Premaratne and M. I. Stockman, Theory and technology of spasers, Adv. Opt. Photonics **9**, 79 (2017).

[36] C. A. Brasil, F. F. Fanchini, and R. de J. Napolitano, A simple derivation of the Lindblad equation, Revista Brasileira de Ensino de Física **35**, 01 (2013).

[37] A. Rivas, A. D. K. Plato, S. F. Huelga, and M. B. Plenio, Markovian master equations: a critical study, New J. Phys. **12**, 113032 (2010).

[38] See Supplemental Material at http://link.aps.org/supplemental/10.1103/PhysRevB.101.245402 for complete numerical simulations of the optically controlled thermal gate system.

[39] L. Kumarapperuma, M. Premaratne, P. K. Jha, M. I. Stockman, and G. P. Agrawal, Complete characterization of the spasing (ll) curve of a three-level quantum coherence enhanced spaser for design optimization, Appl. Phys. Lett. **112**, 201108 (2018).

[40] K. E. Dorfman, P. K. Jha, D. V. Voronine, P. Genevet, F. Capasso, and M. O. Scully, Quantum-Coherence-Enhanced Surface Plasmon Amplification by Stimulated Emission of Radiation, Phys. Rev. Lett. **111**, 043601 (2013).

[41] T. Warnakula, S. D. Gunapala, M. I. Stockman, and M. Premaratne, Cavity quantum electrodynamic analysis of spasing in nanospherical dimers, Phys. Rev. B **100**, 085439 (2019).